Electrochimica Acta 389 (2021) 138554

Contents lists available at ScienceDirect

Electrochimica Acta

journal homepage: www.elsevier.com/locate/electacta

Single-flow multiphase flow batteries: Theory

R. Ronen [a], A.D. Gat [b], M.Z. Bazant [d,e], M.E. Suss [a,b,c,*]

[a] The Nancy & Stephen Grand Technion Energy Program, Technion-Israel Institute of Technology, Haifa 3200003, Israel
[b] Faculty of Mechanical Engineering, Technion-Israel Institute of Technology, Haifa 3200003, Israel
[c] The Wolfson Department of Chemical Engineering, Technion-Israel Institute of Technology, Haifa 3200003, Israel
[d] Department of Chemical Engineering, Massachusetts Institute of Technology, Cambridge, MA 02139, USA
[e] Department of Mathematics, Massachusetts Institute of Technology, Cambridge, MA 02139, USA

ARTICLE INFO

Article history:
Received 31 December 2020
Revised 5 April 2021
Accepted 1 May 2021
Available online 16 May 2021

Keywords:
Energy storage
Aqueous redox flow battery
Zinc-Bromine battery
Multiphase flow
Complexing agents

ABSTRACT

Redox flow batteries are an emerging technology for stationary, grid-scale energy storage. Membraneless batteries in particular are explored as a means to reduce battery cost and complexity. Here, a mathematical model is presented for a membraneless electrochemical cell employing a single laminar flow between electrodes, consisting of a continuous, reactant-poor aqueous phase and a dispersed, reactant-rich nonaqueous phase, and in the absence of gravitational effects. Analytical approximations and numerical solutions for the concentration profile and current-voltage relation are derived via boundary layer analysis. Regimes of slow and fast reactant transport between phases are investigated, and the theory is applied to a membraneless zinc-bromine single-flow battery with multiphase flow. The regime of fast interphase reactant (bromine) transport is characterized by the negligible effect of advection within the cathode boundary layer, leading to a thin boundary layer whose size is largely independent of position, and by relatively high battery current capability. Increasing the nonaqueous (polybromide) phase volume fraction is shown to significantly improve battery performance, as has been observed in recent experiments. For the case of spherical polybromide droplets, the contribution of bromine release from the polybromide phase on the limiting current density becomes negligible for diameters above a critical droplet diameter, when the system can be characterized as having a slow interphase bromine transport. Overall, we show that our analytical approximations agree well with numerical solutions and thus establish a useful theoretical framework for single-flow batteries with multiphase flow .

1. Introduction

A future with green electricity generation has come closer to reality, with the European Green Deal pledging net-zero greenhouse gas emissions by 2050. The transition from fossil fuels to intermittent renewable energy sources, such as solar and wind, requires scalable and cost-effective energy storage solutions for applications such as load leveling and peak shaving [1]. For energy storage at the grid scale, redox flow batteries (RFBs) are promising for systems ranging between 10 kW and 10 MW power delivery [2]. In RFBs, chemical energy is stored in an anolyte solution containing a reductant and catholyte solution with an oxidant. The anolyte and catholyte are stored in separate tanks external to the battery cell, and are pumped into the battery during battery charging or discharging. Within the cell, the anolyte and catholyte are typically separated by an ion exchange membrane to prevent direct mixing of the oxidant and reductant. During discharge of the battery, the oxidant and reductant participate in electrochemical half-reactions at the battery cathode and anode, respectively, converting the stored chemical energy to electricity. Storing chemical energy in tanks allows for a spatial decoupling of the energy stored and power delivered, where energy capacity scales with tank size and power with the stack's electrochemically active area. This architecture can enable facile and cost-effective scaling to grid-scale, can reduce safety considerations, and also enables simpler thermal management [3].

Unlike batteries for portable devices, where gravimetric energy density is a crucial metric, for stationary applications other metrics such as reactant cost and cell power density also play a central role. Thus, while batteries for portable devices generally employ Li-ion chemistry, there is a broader variety of chemistries under active investigation for RFBs, such as all-vanadium [3,4], iron-chromium [3,4], zinc-bromine [4,5], zinc-polyiodide [6], metal-organic [7], such as organic polymer 2,2,6,6-tetramethylpiperidinyl-N-oxyl (TEMPO) or quinone-based [8] and hydrogen-bromine [9]. Another category of RFBs is the hybrid flow battery, where the an-

* Corresponding author.
E-mail address: mesuss@technion.ac.il (M.E. Suss).

https://doi.org/10.1016/j.electacta.2021.138554
0013-4686/

Symbol parameter

E_a^o	Standard anode reduction potential
E_c^o	Standard cathode reduction potential
ε	Polybromide-phase volume fraction
$\bar{c}_{Br_2}^{poly,0}$	Br_2 concentration in the polybromide phase
H	Bromine partition coefficient
D^*	Dispersed-to-continuous phase bromine diffusivity ratio
u	Velocity
U_{avg}	Area-averaged velocity
D_e	Effective diffusion coefficient in the aqueous phase
D_{Br_2}	Bromine molecular diffusion coefficient
K_e	Effective interphase mass transport coefficient
K	Mass-transfer coefficient
a	Particle interfacial area-to-volume ratio
d_p	Particle diameter
$\bar{c}_{Br_2}^{aq}$	Aqueous phase-averaged concentration
$\bar{c}_{Br_2}^{aq,eq}$, $c_{Br_2}^0$	Aqueous phase equilibrium concentration
L	Channel length
H	Channel height
$c_{Br_2}^w$	Bromine concentration along the wall
θ	Scaled bromine concentration
β	Channel aspect ratio
Sh	Reduced Sherwood number
St	Stanton number
Pe	Reduced Peclet number
x_{ent}	Entrance length
N_w	Species flux at the wall
J	Local current density
δ	Dimensionless boundary layer thickness
F	Faraday constant
R	Gas constant
T	Temprature
φ	Electric potential
σ	Ionic conductivity
$\tilde{\varphi}_{cell}$	Dimensionless cell potential
$\tilde{\varphi}_{cell}^0$	Dimensionless standard cell potential
$\tilde{J}_{\text{lim}}$	Dimensionless limiting current

ode's active material is a metal, and thus chemical energy is partially stored in the battery itself. Such systems can achieve among the highest energy densities for RFBs [7], while relying on inexpensive metals. . While RFBs are stationary systems, improving energy density enables cost reductions in balance-of-plant components, as it enables smaller tanks and reduced pumping losses [3]. Technical feasibility of RFBs for grid-scale storage application have been explored for decades, including the "Moonlight project" of 1978 that invested in the zinc-bromine battery [3]. However, commercialization is still an ongoing challenge as the cost of storage must be further reduced. The capital cost target for grid-scale energy storage is $100/kWh, a goal set by the Advanced Research Project Agency-Energy in the USA (ARPA-E) [3,10].

To reduce the cost of RFB stacks, one emerging effort is the development of membraneless cells [7,9,11–15], as the membrane is typically the most expensive component of the stack [10,16]. Membraneless cell designs leverage either laminar flow separation [14,17], use of metal electrodes [7,18], complexing [7,19] or a co-flow of immiscible aqueous and organic solutions [12,20] to separate the oxidant and reductant. The use of complexing agents is typically associated with bromine-based catholytes, and primarily with zinc-bromine RFBs [7,19,21]. Bromine complexing agents (BCAs) are often quaternary ammonium salts which sequester the majority of the bromine in a less-active form within a polybromide phase, thus reducing the crossover of bromine to the zinc electrode [22]. In typical systems, during operation the denser polybromide phase is held within the catholyte tank, and sediments to the bottom of a storage tank while the aqueous phase alone is circulated through the cell [18,19]. Such zinc-bromine batteries use non-selective separators between anolyte and catholyte [18,23]. Recently, Amit et al. showed a proof-of-concept, membraneless and separator-less single-flow system with multiphase flow, where the flow was an emulsion of a dilute, bromine-rich polybromide phase and continuous, bromine-poor aqueous phase [24]. The use of a well-mixed emulsion by Amit et al. is distinct from previous multiphase flow batteries which employed instead two co-flowing immiscible phases [12,20]. The system of Amit et al. showed high current capability of nearly 300 mA/cm^2 for polybromide volume fractions of ~5%, but requires additional optimizations to improve Coulombic efficiency during cycling, and deeper understanding on the mechanisms affecting battery performance.

Theoretical models are important tools towards the optimization of membraneless, single-flow cells relying on BCAs. Previously-developed models focused largely on zinc-bromine batteries with two electrolyte streams separated by a separator and at least one stream containing a complexing agent [5,25–27]. Early work of Evans and White, and Mader and White modeled a zinc-bromine cell with the aqueous phase alone flowing through the cell, and suggested future work could include a bromine-rich phase in the flow [5,27]. An extension of this model was carried out by Kalu and White, who treated the catholyte tank during cell charging as a continuous stirred tank reactor (CSTR) with a mixture of two phases [28]. An empirical correlation was used to describe the distribution ratio of bromine between the two phases in the tank, and the aqueous phase alone flowed through the cell. Koo et al. applied a simpler approach to model a zinc-bromine RFB stack containing a complexing agent in both the anolyte and catholyte, using Ohm's law and charge conservation equations. The cell current density was described by a polynomial functions with several fitting parameters, and the electrochemical cell was modeled using an equivalent circuit [26]. Recent work by Xu et al. modelled a zinc-bromine RFB with two flows through serpentine channels within current collectors, with dilute $ZnBr_2$ electrolytes including BCA in the aqueous phase of the catholyte [25]. Thus, no model to our knowledge has been developed to describe a membraneless, singe-flow battery with multiphase flow.

In membraneless RFBs, mass transport boundary layers form along electrode surfaces and often play a crucial role in cell performance. Boundary layer analysis techniques have been applied to derive simple, approximate solutions of species concentration fields in both flow batteries and other chemical systems, such as those performing chemical separations, chemical reactions, biological reactions, mass transfer from droplets, and interphase transfer in packed-bed reactors [29,30]. For membraneless electrochemical cells with single-phase flow, Braff et al. [11,15] performed a boundary layer analysis leading to analytical expressions capturing cell limiting current and the current-voltage relationship. Nakayama et al. analytically captured the limiting current of electrodialysis cells, and found boundary layer similarity solutions for two asymptotic cases of long and short channels [31]. For single-flow batteries with multiphase flow, the boundary layer at the bromine electrode is expected to be affected by the presence of the polybromide phase in the electrolyte. However, to our knowledge, no battery model has been developed to predict the boundary layer structure along an electrode subjected to multiphase laminar flow, and the connection between this boundary layer and battery performance has not been quantified.

We here extend the theory of membraneless electrochemical systems to include the case of a multiphase flowing electrolyte in

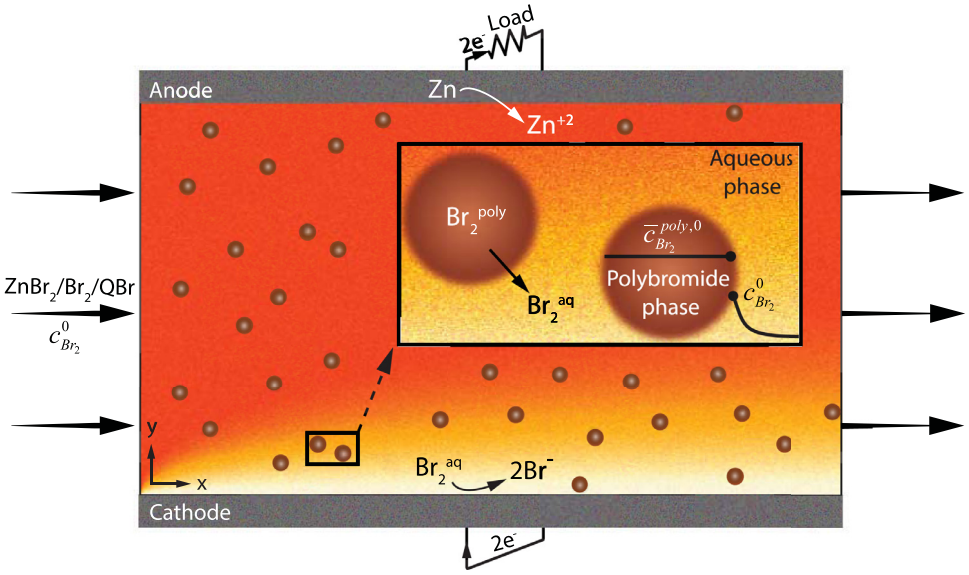

Fig. 1. Schematic of a discharging redox flow battery with a single, multiphase flow between anode and cathode. The flow consists of a continuous, bromine-poor aqueous phase and dispersed, bromine-rich polybromide phase. Inset depicts the assumed bromine concentration profile between a polybromide droplet in the cathode boundary layer and the adjacent aqueous phase.

the absence of gravitational effects. Fig. 1 shows our model system for the case of zinc-bromine chemistry. We investigate the limit where reactant transport between phases is transport-limited, and show this problem is governed by the channel geometrical aspect ratio and two non-dimensional parameters, Peclet number (*Pe*) and Stanton number (*St*). We further obtain analytical solutions in the limit of small and large *St*, elucidate key boundary layer features affecting battery performance, and show good agreement between simple analytical expressions and numerically-generated model results. A specific case of the nonaqueous phase configured as dispersed, spherical-shaped droplets is presented, and we predict a strong effect of droplet size, with up to several orders of magnitude increase in the limiting current density when decreasing droplet size from tens to order one micrometer.

2. Theory

We consider an isothermal membraneless flow battery consisting of two flat electrodes with a single flowing electrolyte between them, operating in a single-pass mode. To illustrate the model, we will utilize zinc-bromine chemistry, where the anode is a zinc metal plate. Thus, the half-reactions considered, for discharge mode, are

$$\text{Anode}: \ Zn_{(s)} \rightleftarrows Zn^{2+}{}_{(aq)} + 2e^- \ E_a^0 = -0.762 \ V \ vs. \ SHE, \tag{1}$$

$$\text{Cathode}: \ Br_{2(aq)} + 2e^- \rightleftarrows 2Br^-_{(aq)} \ E_c^0 = 1.087 \ V \ vs. \ SHE. \tag{2}$$

Where, E_a^o and E_c^o are the standard reduction potentials for the oxidation and reduction half-reactions, respectively, and SHE refers to the standard hydrogen electrode. The electrolyte contains Br_2, a complexing agent, QBr, and $ZnBr_2$ salt, all dissolved in water [5] (see Fig. 1). Q represents the quaternary ammonium cation of the complexing agent. QBr can sequester bromine in the aqueous phase, forming the compound QBr_{2n+1}, which can then separate into a denser polybromide phase,

$$QBr_{(aq)} + nQBr_{2\ (aq)} \rightleftarrows QBr_{2n+1\ (poly)}, \tag{3}$$

where the number of moles of complexed bromine per Q cation is $1 \leq n \leq 3$, where n is an integer [24].

We consider that the single electrolyte flow is a two-phase emulsion characterized by a constant volume fraction, ε, of liquid polybromide phase and $1 - \varepsilon$ of the aqueous phase. We assume the polybromide phase is dilute, discontinuous, and neglect the effect of gravity acting on this phase. During battery operation, bromine is exchanged between the aqueous and polybromide phases. For example, near the cathode during discharge, QBr_3 can de-complex to deliver Br_2 to the locally depleted aqueous phase, in an effort to restore chemical equilibrium [32]. The local rate of transport of Br_2 between phases may depend on the kinetics of the complexation reaction, as well as the impedance to mass transport of Br_2 through the local interfacial region between phases. We here consider the limit of fast complexation in order to simplify the model, and as is often-assumed [9,28,33], although other works estimate the polybromide phase dissociation rate [25].

Generally, the Br_2 concentration in the polybromide phase is about two orders of magnitude higher than in the aqueous phase, and the polybromide phase bromine is relatively electrochemically inactive [19]. Thus, we assume here, for simplicity, that Br_2 concentration in the polybromide phase, $\bar{c}_{Br_2}^{poly,0}$, remains constant throughout the model domain. In other words, we neglect diffusion of bromine within the polybromide phase, and assume that any change in bromine concentration in this phase during single-pass operation is small relative to $\bar{c}_{Br_2}^{poly,0}$. We further assume that the dominant impedance to interphase bromine transport resides outside the polybromide droplet. We expect this assumption to be valid as for the system described here, $H\sqrt{D^*} \gg 1$ [34], where H is the bromine partition coefficient and D^* is the ratio of dispersed to continuous phase bromine diffusivities. D^* is typically order 0.1 as the viscosity in the polybromide phase is about 6 times larger than the aqueous phase [35,36], while H is often very large, typically order 100 for commonly used complexing agents and temperatures [24]. In the aqueous phase, most Br_2 is converted to Br_3^- due to a strong complexation reaction between Br_2 and Br^- (equilibrium constant of 16.7), as well as higher order polybromides, such as Br_5^- to Br_{11}^- [18,37]. For simplicity, we will neglect such complexation reactions in our model, and consider that all bromine in the aqueous phase is contained in either Br_2 or Br^-.

2.1. Analytical approach

For transport problems involving biphasic flow, a common approach to simplifying the microscopic transport equations is to re-cast them in terms of volume-averaged variables [26,38–41]. Whitaker, followed by Gray rigorously derived and applied these multi-phase transport equations for problems involving interphase mass transport [38,39]. We apply such a framework to study the single-flow battery with multiphase flow during battery discharge at the limiting current. We assume fully- developed flow, steady state, and a two-dimensional concentration field. The resulting species balance equation is

$$u\frac{\partial \bar{c}^{aq}_{Br_2}}{\partial x} = D_e\left(\frac{\partial^2 \bar{c}^{aq}_{Br_2}}{\partial x^2} + \frac{\partial^2 \bar{c}^{aq}_{Br_2}}{\partial y^2}\right) - K_e\left(\bar{c}^{aq}_{Br_2} - \bar{c}^{aq,eq}_{Br_2}\right). \tag{4}$$

For the limit of a dilute polybromide phase, we can assume fully-developed Poiseuille flow within the channel, so that $u(y) \approx 6U_{avg}(y/H - (y/H)^2)$, where U_{avg} is the area-averaged velocity in the channel. The effective diffusion coefficient in the aqueous phase is given by $D_e = (1-\varepsilon)D_{Br_2}$, where D_{Br_2} is the bromine molecular diffusion coefficient [42]. To account for the averaged mass transport of bromine between phases, the effective interphase mass transport coefficient is given by $K_e = (1-\varepsilon)aK$, where K is a mass-transfer coefficient which depends on the shape and characteristic size of the local polybromide-phase particles [43], and a is the interfacial area per m^3. For spherical particles, $a = 6\varepsilon/d_p$, where d_p is the particle diameter. We assume that K is constant, meaning we assume a uniform shape and size of polybromide phase particles throughout the model domain. Here, $\bar{c}^{aq}_{Br_2}$ is the aqueous phase-averaged concentration, and $\bar{c}^{aq,eq}_{Br_2}$ is the concentration of the aqueous phase when the polybromide and aqueous phases are in mutual equilibrium [38]. We take $\bar{c}^{aq,eq}_{Br_2}$ as the bromine concentration of the incoming flow, so that $\bar{c}^{aq,eq}_{Br_2} = c^0_{Br_2}$. In assuming constant ε, we neglect the effect of gravity acting on the denser polybromide phase, which is justifiable in the limit of small density differences between phases, small polybromide particle sizes, or large flow velocities [50]. Future work can extend the model presented here to account for additional phenomena affecting the bromine boundary layer in certain operational regimes, such as polybromide sedimentation, changing polybromide-phase droplet size due to bromine depletion, or coalescence of droplets in flow.

At the limiting current, the boundary conditions are

$$\bar{c}^{aq}_{Br_2}(0,y) = c^0_{Br_2},\quad \bar{c}^{aq}_{Br_2}(x,0) = 0,\quad \bar{c}^{aq}_{Br_2}(x,H) = c^0_{Br_2},\quad \left.\frac{\partial \bar{c}^{aq}_{Br_2}}{\partial x}\right|_{x=L} = 0. \tag{5}$$

Where the boundary condition at $x = L$ is appropriate at the limit of high Pe. To develop a non-dimensional version of the species balance equation, we define scaled concentration as $\theta \equiv (\bar{c}^{aq}_{Br_2} - c^0_{Br_2})/(c^w_{Br_2} - c^0_{Br_2}) = 1 - \bar{c}^{aq}_{Br_2}/c^0_{Br_2}$, where the bromine concentration at the wall is $c^w_{Br_2} = 0$ at the limiting current. Coordinates are scaled to $\tilde{x} = x/L$ and $\tilde{y} = y/H$, and we define a velocity scale as $U = 6U_{avg}$ Scaling of Eq. (4) with these parameters yields

$$\frac{1}{St}\left(\tilde{y} - \tilde{y}^2\right)\frac{\partial \theta}{\partial \tilde{x}} = \frac{\beta}{Sh}\left(\frac{1}{\beta^2}\frac{\partial^2\theta}{\partial \tilde{x}^2} + \frac{\partial^2\theta}{\partial \tilde{y}^2}\right) - \theta, \tag{6}$$

where $\beta = L/H$ is the channel aspect ratio, $Sh = K_eLH/D_e$ is the reduced Sherwood number, and $St = K_e/(U/L)$ is the Stanton number which is the ratio between Sh and the reduced Peclet number, $Pe = UH/D_e$.

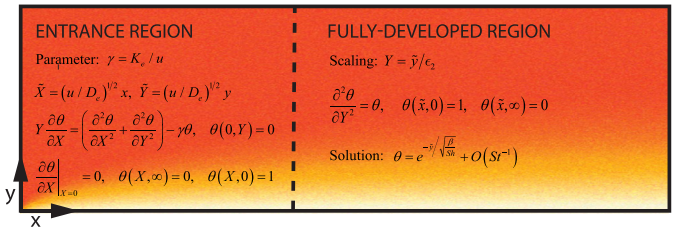

Fig. 2. Schematic showing the investigated geometric regions along the cathode side of the flow, for the regime of St >>1. The equations governing the concentration field and the analytical solution are shown for the fully-developed region, and in the entrance region the analytical solution is given by Eqs. (21) and (22).

2.1.1. Regime of fast interphase mass transfer ($St >> 1$, $St >> \beta/Pe$)

We define $\epsilon_1 = 1/St$, $\epsilon_2 = \beta/PeSt$, where for $St >> 1$, $\epsilon_1 \ll 1$, and for $St >> \beta/Pe$, $\epsilon_2 \ll 1$. In this case, the small parameter ϵ_1 multiplies the highest derivative in x, suggesting a boundary layer near $x = 0$. In addition, the small parameter, ϵ_2, is a prefactor of the highest-order term suggesting another boundary layer near $y = 0$. We focus our boundary layer analysis on two regions of the channel: an entrance region containing the developing bromine boundary layer, and a fully-developed region containing the developed bromine boundary layer (see Fig. 2). For completeness, we also analyze two regions outside the bromine boundary layer, the region outside the bromine boundary layer but near to the inlet at $x = 0$, and the region outside the boundary layer and far from the inlet.

For the latter region, using the same scaling as in Eq. (6), and neglecting the x-direction diffusion in the long channel [44], we obtain

$$\epsilon_1\left(\tilde{y} - \tilde{y}^2\right)\frac{\partial\theta}{\partial\tilde{x}} = \epsilon_2\frac{\partial^2\theta}{\partial\tilde{y}^2} - \theta. \tag{7}$$

In this region, both advection and diffusion are negligible compared to interphase mass transfer, and a trivial solution is obtained, $\theta = 0$. For inlet region, but outside the bromine boundary layer, we rescale x as$X = \tilde{x}/\epsilon_1$ to obtain

$$\left(\tilde{y} - \tilde{y}^2\right)\frac{\partial\theta}{\partial X} = \epsilon_2\left(\frac{1}{(\epsilon_1\beta)^2}\frac{\partial^2\theta}{\partial X^2} + \frac{\partial^2\theta}{\partial\tilde{y}^2}\right) - \theta. \tag{8}$$

As ϵ_1 and imposing $St \ll \beta Pe$, we can neglect the diffusion terms. Solving the resulting equation using the boundary condition $\theta(0,\tilde{y}) = 0$, we obtain the trivial solution, $\theta = 0$. Although we note that if the inlet bromine concentration did not match the equilibrium aqueous-phase bromine concentration, then Eq. (8) would yield a non-trivial solution.

For the fully-developed region, scaling Eq. (6) with $Y = \tilde{y}/\epsilon_2$ yields

$$\epsilon_1\epsilon_2\left(Y - \epsilon_2 Y^2\right)\frac{\partial\theta}{\partial\tilde{x}} = \frac{\partial^2\theta}{\partial Y^2} - \theta, \tag{9}$$

which can be solved exactly by Finite Fourier Transform in the full domain as an infinite series in terms of Graetz functions, which capture the effect of non-uniform advection in mass transfer [45].

As we here restrict ourselves to the limit where ϵ_1 is small, we can neglect advection, so the simplified equation and boundary conditions are

$$\frac{\partial^2\theta}{\partial Y^2} = \theta,\quad \theta(\tilde{x},0) = 1,\quad \theta(\tilde{x},\infty) = 0. \tag{10}$$

Similar boundary layer behavior, where flow velocity does not affect the boundary layer concentration field, has been previously observed by Chambre and Young [46] and Bird et al. [30] for single-phase flow over a reacting flat plate. The solution to Eq. (10) is

$$\theta = e^{-\tilde{y}/\sqrt{\frac{\beta}{Sh}}} + O\left(St^{-1}\right). \tag{11}$$

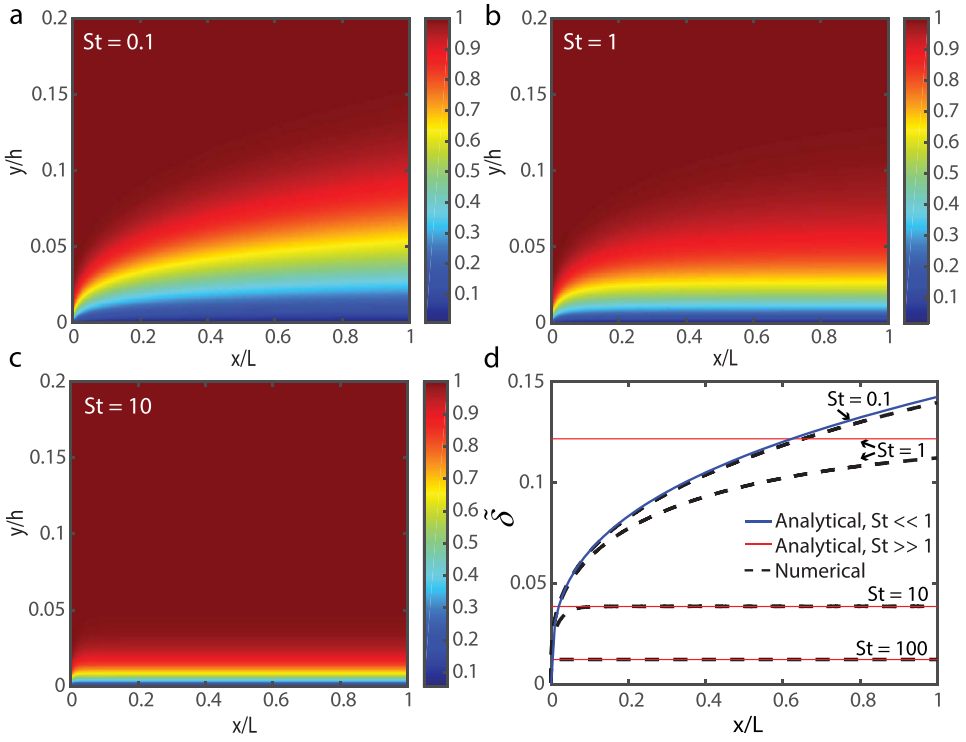

Fig. 3. (a), (b), (c) Predicted concentration fields of the numerical model for Stanton numbers (St) of 0.1, 1 and 10, respectively. (d) Boundary layer thickness predicted by the numerical model (dashed lines) and the analytical model for various Stanton numbers (red and blue curves) (For interpretation of the references to color in this figure legend, the reader is referred to the web version of this article.).

The dimensional concentration is

$$\tilde{c}^{aq}_{Br_2} = c^0_{Br_2}\left(1 - e^{-\tilde{y}/\sqrt{\frac{\beta}{Sh}}} + O\left(St^{-1}\right)\right). \tag{12}$$

The first term in the solution given in Eq. (12) is the leading order solution, while the next term is the correction to the leading order, which is on the order of St^{-1}. However, we will not derive this correction term here, as our comparison of the leading order solution to numerical simulation results demonstrated negligible error throughout the boundary layer, except within the small entrance region where advection cannot be neglected (see Fig. 3). The order-of-magnitude of the entrance length, x_{ent}, can be estimated by rescaling $\hat{x} = \tilde{x}/\delta_x$, where $\delta_x \equiv x_{ent}/L$. By substituting this scaling into Eq. (6), we obtain

$$\frac{1}{St\delta_x}\tilde{y}\frac{\partial\theta}{\partial\hat{x}} = \frac{\beta}{Sh}\frac{\partial^2\theta}{\partial\tilde{y}^2} - \theta. \tag{13}$$

When neglecting axial diffusion, Eq. (13) yields that the entrance length, δ_x, scales as St^{-1}, and its dimensionless thickness in the flow direction is given as

$$x_{ent}/L \sim St^{-1} = (U/L)/K_e. \tag{14}$$

From Eq. (12), we can obtain a dimensionless bromine boundary layer thickness, defined as the $\tilde{y}$ position where the aqueous-phase bromine concentration reaches 99% of the inlet value, as

$$\tilde{\delta} = 4.6\sqrt{\beta/Sh}. \tag{15}$$

The boundary layer in this regime is typically thin, as for the representative parameters listed in Table 2, $\tilde{\delta} = 0.015$. At the cathode, the flux of bromine to the plate is entirely diffusive, and is maximized at the limiting current. This flux is given by

$$N_w = \frac{D_e c^0_{Br_2}}{H}\left.\frac{\partial\theta}{\partial\tilde{y}}\right|_{\tilde{y}=0}. \tag{16}$$

We now apply Faraday's law to relate bromine flux to local current density, J, at the cathode, and define dimensionless current density as $\tilde{J} = J/J_s$, where $J_s = nD_eFc^0_{Br_2}/H$, and $n = 2$ is the number of electrons transferred for the reacting bromine. The limiting current density in the fully-developed region can be written as

$$\tilde{J}_{\text{lim}} = \frac{H}{nD_eFc^{aq,0}_{Br_2}}J = \left.\frac{\partial\theta}{\partial\tilde{y}}\right|_{\tilde{y}=0} = \sqrt{Sh/\beta}. \tag{17}$$

Turning our attention to the entrance region, here the axial diffusion term cannot be omitted at the leading edge of the plate [44]. However, in this region the cathode boundary layer is very thin relative to the channel height, thus we can linearize the velocity field to $u(y) \approx 6U_{avg}y/h$ using the Lévêque approximation [45]. Introducing the dimensionless variables, $\tilde{X} = (u/D_e)^{1/2}x$, $\tilde{Y} = (u/D_e)^{1/2}y$ and $\gamma = K_e/u$ to scale Eq. (4), we obtain [44]

$$\tilde{Y}\frac{\partial\theta}{\partial\tilde{X}} = \left(\frac{\partial^2\theta}{\partial\tilde{X}^2} + \frac{\partial^2\theta}{\partial\tilde{Y}^2}\right) - \gamma\theta, \tag{18}$$

and the boundary conditions are

$$\theta\left(0,\tilde{Y}\right) = 0, \quad \theta\left(\tilde{X},\infty\right) = 0, \quad \theta\left(\tilde{X},0\right) = 1. \tag{19}$$

We can utilize another restriction at the inlet,

$$\left.\frac{\partial\theta}{\partial\tilde{X}}\right|_{\tilde{X}=0} = 0, \tag{20}$$

In order to simplify the Laplace transformation used to solve Eq. (18) [44]. In Eq. (18), all terms are of the same order of magnitude, and this problem is mathematically analogous to that examined in Apelblat for a system with a homogeneous chemical reaction and Couette flow [44]. In the latter work, two cases were solved for analytically, those with and without axial diffusion. For the case without axial diffusion, utilizing the solution from Apelblat for diffusive flux (Eq. (47)a of Ref. [44]), and Faraday's law, we derive the

dimensionless limiting current density for our battery in the entrance region,

$$\tilde{J}_{\lim} = \left(1 + \frac{\beta^{-1/2}}{\pi^2}\int_0^\infty \frac{\exp\left(-u\sqrt{6Pe}\beta\tilde{x}\right)du}{u^{2/3}\left[{A_1}^2\left(-\beta/u^{2/3}\right) + {B_1}^2\left(-\beta/u^{2/3}\right)\right]}\right)\sqrt{\frac{Sh}{\beta}}. \quad (21)$$

We further derive the limiting current density when including axial diffusion, using the available analytical solution for diffusive flux (Eq. (46) of Ref. [44]), which yields

$$\tilde{J}_{\lim} = \left(1 + \frac{\beta^{-1/2}}{\pi^2}\int_0^\infty \frac{\exp\left(-u\sqrt{6Pe}\beta\tilde{x}\right)du}{u^{2/3}\left[{A_1}^2\left(u^{1/3}(u-\beta/u)\right) + {B_1}^2\left(u^{1/3}(u-\beta/u)\right)\right]}\right)\sqrt{\frac{Sh}{\beta}}. \quad (22)$$

2.1.2. Regime of slow interphase mass transfer (St << 1)

This limit depicts an undesirable scenario for batteries with multiphase flow, but may occur in practice, for example for polybromide-phase droplets with large characteristic size. In such a regime, there is no longer an entrance region and developed region of the bromine boundary layer, as the boundary layer continues to develop throughout the channel. Rewriting Eq. (6), and neglecting axial diffusion, we obtain

$$\left(\tilde{y} - \tilde{y}^2\right)\frac{\partial\theta}{\partial\tilde{x}} = \frac{\beta}{Pe}\frac{\partial^2\theta}{\partial\tilde{y}^2} - St\theta,\ \theta(0,\tilde{y}) = 0,\ \theta(\tilde{x},0) = 1,\ \theta(\tilde{x},\infty) = 0. \quad (23)$$

Defining $\epsilon \equiv St$, we investigate the regime where $\beta/Pe \ll \epsilon$. For the outer region, outside the bromine boundary layer, Eq. (23) becomes

$$\left(\tilde{y} - \tilde{y}^2\right)\frac{\partial\bar{\theta}}{\partial\tilde{x}} = -\epsilon\bar{\theta}, \quad (24)$$

where dimensionless concentration in the outer region is denoted as $\bar{\theta}$. We find from Eq. (24) that the solution is $\bar{\theta} = 0$, and as expected it cannot satisfy the boundary condition at $\tilde{y} = 0$.

For the inner region, within the boundary layer, not only is St small, but there is another small parameter, the dimensionless boundary layer thickness δ. The balance between advection and diffusion fluxes lead to the inner coordinate $\tilde{Y} = \tilde{y}/\delta$, where $\delta = (\beta/Pe)^{1/3}$. By re-scaling Eq. (23), and since $\delta \ll 1$, it becomes

$$\tilde{Y}\frac{\partial\hat{\theta}}{\partial\tilde{x}} = \frac{\partial^2\hat{\theta}}{\partial\tilde{Y}^2} - \frac{St}{\delta}\hat{\theta}, \quad (25)$$

where the inner region scaled concentration is denoted as $\hat{\theta}$. When $St/\delta \ll 1$, the parameter ϵ is small everywhere, in both the inner and outer regions. We will solve for the leading order solution, $\hat{\theta}_0$, where $St = 0$, which yields

$$\tilde{Y}\frac{\partial\hat{\theta}_0}{\partial\tilde{x}} = \frac{\partial^2\hat{\theta}_0}{\partial\tilde{Y}^2},\quad \hat{\theta}_0\left(0,\tilde{Y}\right) = 0,\quad \hat{\theta}_0(\tilde{x},0) = 1,\quad \hat{\theta}_0(\tilde{x},\infty) = 0. \quad (26)$$

This problem was solved by Lévêque [44], and the solution utilized by Braff et al. for battery limiting current for the case of single-phase flow between electrodes (Eq. (16) in Ref. [11]). The solution is

$$\hat{\theta}_0 = 1 - \Gamma\left(\frac{Pe\,\tilde{y}^3}{9\beta\,\tilde{x}}, \frac{1}{3}\right). \quad (27)$$

where, the incomplete gamma function is defined as $\Gamma(s,a) = \left(\int_0^s e^{-t}t^{a-1}dt\right)/\left(\int_0^\infty e^{-t}t^{a-1}dt\right)$. By matching the outer and inner solution, we obtain the aqueous-phase bromine concentration as

$$\bar{c}^{aq}_{Br_2} \sim c^0_{Br_2}\,\Gamma\left(\frac{Pe\,\tilde{y}^3}{9\beta\,\tilde{x}}, \frac{1}{3}\right). \quad (28)$$

The dimensionless boundary layer thickness for this solution is

$$\tilde{\delta}(\tilde{x}) = 2.92\sqrt[3]{\beta\tilde{x}/Pe}. \quad (29)$$

The resulting dimensionless limiting current density expression is analogous to Eq. (17) in Ref. [11], and is

$$\tilde{J}_{\lim}(\tilde{x}) = \sqrt[3]{\frac{3Pe}{\beta\tilde{x}}}\frac{1}{\Gamma(1/3)}. \quad (30)$$

The averaged limiting current along the cathode is

$$\overline{J}_{\lim} = 3\sqrt[3]{\frac{3Pe}{8\beta}}\frac{1}{\Gamma(1/3)} \quad (31)$$

2.1.3. Under-limiting current

Analytical solutions obtained here for the limiting current can be utilized to develop equilibrium current-voltage expressions for under limiting currents, when assuming negligible activation overpotential losses, mass transfer limitation due to bromine depletion, and one-dimensional current [11,25,47,48]. In zinc-bromine batteries, the activation overpotentials are usually negligible, since the reactions at the electrodes are kinetically fast [11]. A local current-voltage relation can be expressed in terms of dimensionless potential $\tilde{\varphi} = F\varphi/RT$ and conductivity $\tilde{\sigma} = RT\sigma/nD_{Br_2}F^2c^0_{Br_2}$ as

$$\tilde{\varphi}_{cell} = \tilde{\varphi}^0_{cell} + \frac{1}{2}\ln\left(\theta(\tilde{x})\right) - \tilde{J}(\tilde{x})/\tilde{\sigma}. \quad (32)$$

Here, the dimensionless cell potential is $\tilde{\varphi}_{cell}$ and the dimensionless standard cell potential is $\tilde{\varphi}^0_{cell}$. The local current density along the electrode can be expressed as,

$$\tilde{J}(\tilde{x}) = (1 - \theta(\tilde{x}))\tilde{J}_{\lim}(\tilde{x}). \quad (33)$$

Substituting the result into Eq. (32), and using the analytical limiting current expressions obtained in previous sections, we obtain the following current-voltage relation [11],

$$\tilde{\varphi}_{cell} = \tilde{\varphi}^0_{cell} + \frac{1}{2}\ln\left(1 - \tilde{J}(\tilde{x})/\tilde{J}_{\lim}(\tilde{x})\right) - \tilde{J}(\tilde{x})/\tilde{\sigma}. \quad (34)$$

2.2. Numerical approach

The dimensionless species balance equation solved for numerically is Eq. (4). At the inlet, outlet and cathode, we use dimensionless versions of the boundary conditions specified in Eq. (5). At the anode, we set zero bromine flux,

$$\left.\frac{\partial\bar{c}^{aq}_{Br_2}}{\partial y}\right|_{y=H} = 0. \quad (35)$$

These equations were solved using Comsol Multiphysics 5.4 software.

3. Results and discussions

To study the mass transport boundary layer forming at the cathode during discharge, and validate our analytical solutions, we numerically solved the model given by Eqs. (4), (5) for values of parameters listed in Table 2 and at the limiting current. The simulation was solved for an electrolyte with σ = 100 mS/cm, which is about the conductivity of 2 M $ZnBr_2$, and $c^0_{Br_2} = 12mM$, which is about the aqueous phase concentration for typically used BCAs [35,49]. Fig. 3 shows the solution to the numerical model and comparisons with the analytical results. Here we varied the St number, while Pe was held constant. The predicted concentration field is shown in Fig. 3a to 3c for St = 0.1, 1, and 10, respectively. In all cases, a bromine-depleted boundary layer develops along the cathode as bromine is consumed during cell discharge. In Fig. 3a, for St = 0.1, representing the regime of slow flow interphase mass

Table 1
Summary of the main analytical solutions obtained at the small and large *St* limits.

	$St \ll 1$	$St \gg 1$
Bromine concentration	$\tilde{c}^{aq}_{Br_2}(\tilde{x},\tilde{y}) = c^0_{Br_2}\left(\Gamma\left(\frac{Pe\,\tilde{y}^3}{9\beta\,\tilde{x}},\frac{1}{3}\right)+O(St)\right)$	$\tilde{c}^{aq}_{Br_2}(\tilde{y}) = c^0_{Br_2}(1-e^{-\tilde{y}/\sqrt{\beta/Sh}}+O(St^{-1}))$
Current density	$\tilde{J}_{\lim}(\tilde{x}) = \sqrt[3]{\frac{3Pe}{\beta\tilde{x}}}\frac{1}{\Gamma(1/3)}$	$\tilde{J}_{\lim} = \sqrt{Sh/\beta}$
Boundary layer thickness	$\tilde{\delta}(\tilde{x}) = 2.92\sqrt[3]{\beta\tilde{x}/Pe}$	$\tilde{\delta} = 4.6\sqrt{\beta/Sh}$

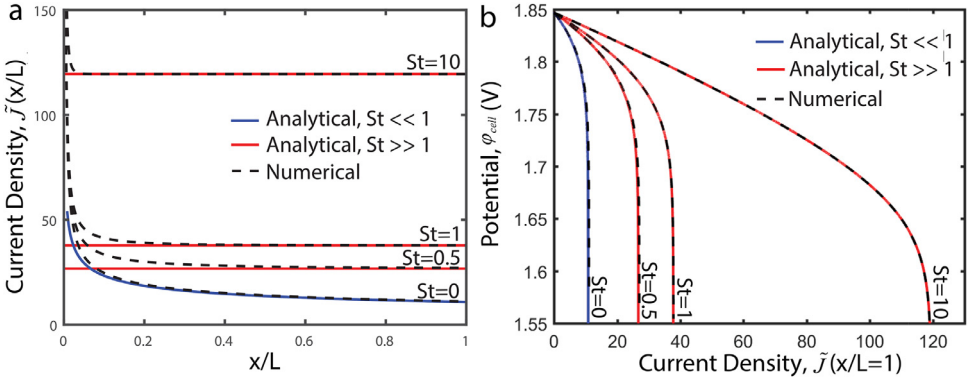

Fig. 4. (a) Comparisons between the numerical model results (dashed curves) and the analytical model results (blue and red curves) for dimensionless current density along the cathode of the battery. (b) Comparisons between numerical model results (dashed curves) and analytical model results (red and blue curves) for cell voltage versus current density. In all cases, the analytical model captures numerical results well for Stanton number (*St*) of order unity or higher (For interpretation of the references to color in this figure legend, the reader is referred to the web version of this article.).

transport, we observe classic laminar-flow boundary layer behavior, with a thin boundary layer at the leading edge which grows as approximately $x^{1/3}$ [11,44], reaching 0.1425 y/h at the trailing edge of the cathode. In Fig. 3b, for $St = 1$, a relatively thinner boundary layer is obtained, exhibiting weaker growth with x, and reaching only 21% of the boundary layer thickness at the trailing edge of the $St = 0.1$ case. In Fig. 3c, for $St = 10$, a yet-thinner boundary layer is obtained with 0.0385 y/h at the trailing edge of the plate, and the boundary layer is of approximately constant thickness after a short entrance length. The entrance length seen in the numerical model results of Fig. 3c is ~0.1 x/L, which matches predictions of Eq. (14).

For large *St*, at constant *Pe*, boundary layer thickness predicted by the analytical model of the fully-developed region is proportional to *St* according to $\tilde{\delta}_1/\tilde{\delta}_2 \propto \sqrt{St_2/St_1}$ (see Eq. (15)). Thus, faster mass transfer between the phases enables a thinner boundary layer and faster bromine transport to the cathode. In Fig. 3d, we compare the numerically-predicted boundary layer thickness to analytical results given by Eq. (15) for large *St* and Eq. (29) for small *St* (Table 1). For $St >> 1$, the numerical model predicts an approximately uniform boundary layer thickness, largely independent of x, which agrees well with the analytical solution, except in the the entrance length in which diffusion, advection and interphase mass-transfer all affect the solution. For $St = 0.1$, the boundary layer grows markedly as ~$x^{1/3}$, and the numerical and analytical models are in good agreement for this regime. For unity *St*, neither the large nor small *St* analytical expressions capture the numerical solution. Thus, overall, the analytical models developed in the Theory section and shown in Table 1, are sufficient to describe the bromine boundary layer, except when *St* is on the order of unity, where the numerical model is required.

In Fig. 4, we link boundary layer behavior and the resulting limiting current, $\tilde{J}_{\lim}$, to battery performance, using Eq. (34). In Fig. 4a, we plot dimensionless current density, $\tilde{J}$, versus position in the channel, x/L, at the limiting current. Plots are for numerical (dashed curves) and analytical models, and for large *St* (red curves) and small *St* (blue curve) (Table 1). At the cathode's leading edge, we observe a rapid drop in current density along the length of the channel in all cases of the numerical model results, from approximately $2000J_s$ to several hundred or ten times J_s depending on the *St* number. This large drop in current density in x is due to the rapid growth of the bromine boundary layer at the leading edge, even for large *St*. For fast interphase mass transfer, $St >> 1$, the current density predicted by the numerical model is well-captured by the analytical solution for the fully-developed region, but not at the entrance region of the channel, as expected. For slow mass transfer, $St << 1$, the current density decreases with x all along the cathode, and is well described by the analytical solution for $St << 1$. For $St \sim 1$, we observe features of both large and small *St* regimes. For example, for $St = 0.5$, the numerically-predicted current density is invariant past about 0.5 x/L, and this location is captured by the analytical solution of the fully-developed region.

Fig. 4b shows the predicted cell voltage as a function of the cathode current density at $x/L = 1$, for varying *St* between 0 to 100. As can be seen, increased *St* results in improved battery performance via reduced voltage losses and improved cell limiting current. As all these predictions utilized the same value of electrolyte ionic conductivity Table 2), the improved performance is due to the enhanced bromine transport to the cathode for higher *St*. For large *St*, we observe that the thinner boundary layer seen in Fig. 3d corresponds to higher limiting current density in Fig. 4b. Further, we observe that there is no significant deviation between numerical and analytical results. In Fig. 4a, significant deviations between numerical and analytical results were observed mainly in the inlet region, far from $x/L = 1$. We conclude that at these conditions, current-voltage relationships far from the leading edge can be captured using the relatively simple analytical expressions presented in Table 1. For large *St*, the analytical solution of Apelblat can be used to capture the entrance region [44], see Eqs. (21) and ((22).

In Fig. 5, we show the effect of polybromide phase volume fraction, ε, on the cell current. For this, we assume spherical-shaped polybromide droplets with $K = 1.7\times10^{-4}$ m/s and a diameter of $d_p = 10\ \mu$m. Fig. 5a, shows the predicted current density along the channel at the limiting current condition, for varying ε between 0

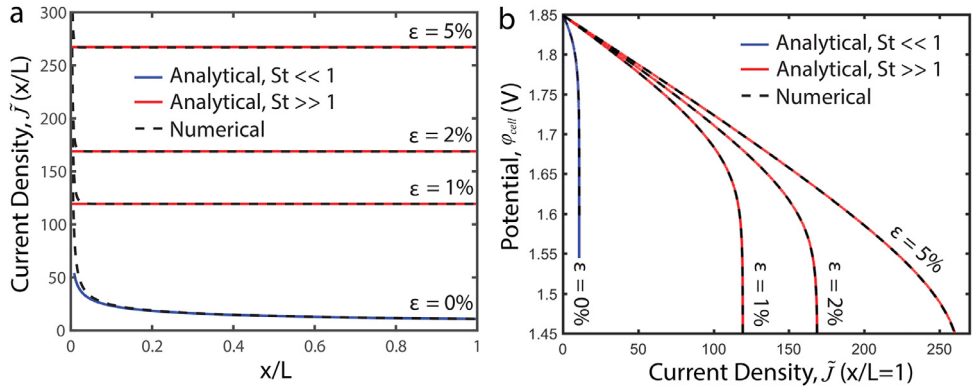

Fig. 5. Predicted polybromide phase volume fraction effect on battery performance showing numerical (dashed lines) and analytical (red and blue solid lines) solutions. (a) Local dimensionless current density along the channel at the limiting current, and (b) cell voltage *versus* local current density at $\tilde{x}/L = 1$ (For interpretation of the references to color in this figure legend, the reader is referred to the web version of this article.).

Table 2
Model parameters and dimensionless variables used in the numerical model solution.

Parameter	Symbol	Value
Bromine diffusivity	D_{Br_2}	1.15×10^{-9} [m^2/s]
Channel height	H	0.004 [m]
Channel length	L	0.095 [m]
Channel width	W	0.009 [m]
Volumetric electrolyte flow rate	Q	20 [ml/min]
Inlet aqueous bromine concentration	$c^0_{Br_2}$	12 [mM]
Conductivity	σ	100 [mS/cm]
Standard cell potential	φ^0_c	1.849 [V]

Dimensionless variables	Symbol	Scale
Position	$(\tilde{x}, \tilde{y})$	$(x/L, y/h)$
Concentration	θ	$\frac{\bar{c}^{aq}_{Br_2} - \bar{c}^{aq,0}_{Br_2}}{c^w_{Br_2} - c^0_{Br_2}} = 1 - \frac{\bar{c}^{aq}_{Br_2}}{c^0_{Br_2}}$
Potential	$\tilde{\varphi}$	$\varphi/(RT/F)$
Current density	$\tilde{J}$	J/J_s

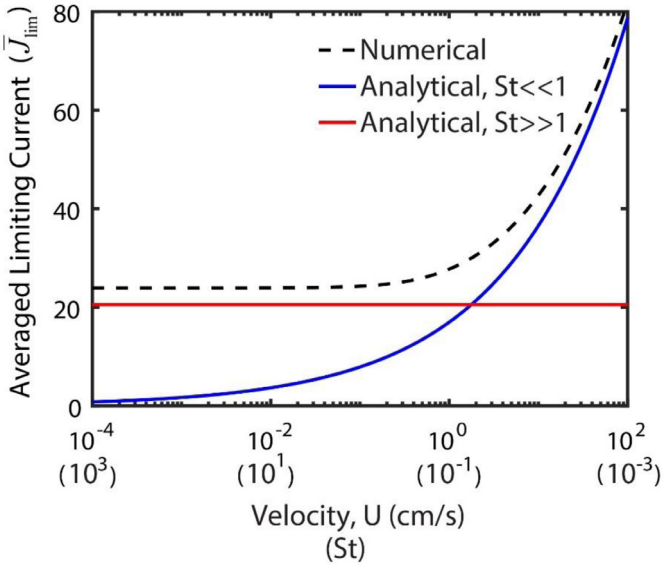

Fig. 6. Predicted numerical (dashed curve) and analytical (solid curves) dimensionless cathode area-averaged limiting current density, $\bar{J}_{lim}$, plotted against flow velocity, U, for a constant Sherwood number, $Sh = 10^4$. The x-axis also shows the St number associated with each velocity (For interpretation of the references to color in this figure legend, the reader is referred to the web version of this article.).

to 5%. Plots are for numerical (dashed curves) and analytical models for large *St* (red curves) and small *St* (blue curve). As can be seen, increasing ε, results in higher limiting current and shorter entrance length. For example, $\varepsilon = 1\%$ yields ~11 times higher current density compared to a system where $\varepsilon \sim 0$. Increasing ε from 1 to 5% improved limiting current by more than two-fold, which agrees well with the rise in cell limiting current observed experimentally by Amit et al. in Ref. [24]. In Fig. 5b, we show predictions of battery voltage versus outlet current during discharge varying for ε. At $\varepsilon = 0$ the cathode is starved of bromine and we observe a severe mass transport limitation even at moderate currents of ~$10J_s$. By introducing $\varepsilon = 1\%$, the limiting current improved by over an order of magnitude, and at $\varepsilon = 5\%$ the limiting current increased by more than twenty-fold. Thus, our model predicts that ε plays a crucial role in battery current capability. The polybromide phase enables improved bromine transport to the cathode while maintaining a low aqueous phase bromine concentration of ~ 10 mM, minimizing anode corrosion by bromine.

In Fig. 6, we examine the effect of electrolyte velocity on the predicted area-averaged cathode limiting current density, which is accomplished by holding *Sh* constant at $1{\cdot}10^4$ and ε at 5% and ε, while *Pe* is varied. The *St* numbers associated with the velocities investigated are shown in parentheses along the *x*-axis, where *St* ranges between 10^{-3} to 10^3. Both numerical (dashed curve) and analytical results for $St << 1$ (red curve) and $St >> 1$ (blue curve) are shown (Table 1). At low velocities, which is associated with large *St*, we can see that the averaged limiting current is largely independent of the electrolyte velocity. This is unlike single-phase membraneless batteries, where limiting current scales as $\tilde{J}_{lim} \propto \sqrt[3]{Pe}$ [11], and is due to the insignificant effect of advection in the fully-developed region of the multiphase flow battery. Instead our $St >> 1$ analytical model predicts the limiting current density is affected by *Sh* and cell geometry according to Eq. (17). At intermediate velocities, associated with $St \sim 0.1$ to 1, a transition zone is observed in the numerical model where velocity begins to affect the predicted limiting current, but is not yet well-captured by the low *St* analytical solution. Increasing velocity yet further results in improved limiting current, and a scaling of $\tilde{J}_{lim} \propto \sqrt[3]{Pe}$ as predicted by the low *St* analytical solution (Eq. (30)). We can also see in Fig. 6, at low velocities, a discrepancy between numerically calculated limiting current and the $St >> 1$ analytical solution for the fully-developed region, a deviation which is ~14%. We attribute this to the entrance region, where the analytical model underpredicts current density, as this region is not captured in the fully-developed region solution. Overall, the predictions of the effect of velocity on limiting current in Fig. 6 can in the future be compared to experimental results from the single-flow multiphase flow bat-

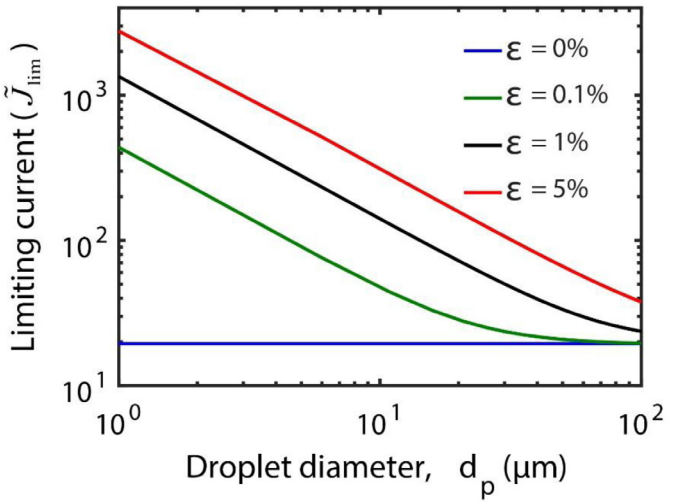

Fig. 7. Predicted limiting current density vs. polybromide phase droplet diameter, d_p, at various polybromide phase volume fractions, ε.

tery, and can allow for extraction of key parameters such as K from model-to-data-fitting.

We now develop further the specific case of spherical polybromide droplets. Since the viscosity of the polybromide phase inside the droplets is typically much greater than the viscosity of the aqueous phase [51,52], the droplets can be treated as solid-like spheres flowing in suspension [53]. We can define Pe_c as $Pe_c = d_p v_t / D_{Br_2}$, where d_p is the droplet diameter, v_t is the droplet terminal velocity and D_{Br_2} is the solute diffusivity in the continuous phase. For stable emulsions, and creeping flow about the particle, $Sh_c = 1 + (1 + Pe_c)^{1/3}$ [34], and the Sherwood number is $Sh_c = K d_p / D_{Br_2} = 2$. Thus, the mass-transfer coefficient between the phases is $K = 2D_{Br_2}/d_p$. This relation is utilized in the numerical model for generating Fig. 7.

Fig. 7 presents the predicted limiting current density, $\tilde{J}_{lim}$, as a function of droplet diameter, d_p, for various polybromide phase volume fractions, ε, from 0 to 5%. We observe that increasing d_p results in lower current density for all finite values of ε. Further, $\tilde{J}_{lim}$ reaches an asymptotic minimum at the limit of large d_p, where this minimum is predicted by the small St analytical expression (Eq. (31), Table 1). We observe that for higher polybromide phase volume fraction, this asymptotic limit is reached at larger droplets. For example, for $\varepsilon = 0.1\%$ the limit is reached at about $d_p = 80$ μm, and for $\varepsilon = 1\%$ this limit is reached closer to $d_p = 100$ μm. Thus, when the droplet reaches this critical size, the contribution of bromine release from the polybromide phase on the limiting current density becomes negligible. This is because of the role of the droplet's surface area to volume ratio, a, in the mass transfer between the phases, (Eq. (4)). For spherical particles, the interfacial flux is linearly proportional to the square root of the droplet diameter. This suggests that injecting into the battery an emulsion with very fine polybromide particles can allow for improved bromine transport to the cathode and cell current capability.

4. Conclusion

We developed analytical and numerical theory for a single-flow battery leveraging multiphase flow. We here restricted the model to the case of a dilute emulsion unaffected by gravity, but in the future such assumptions can be relaxed if needed. We illustrate the theory using zinc-bromine battery chemistry, and showed that battery performance is crucially dependent on the properties of the cathode boundary layer. We show that simple analytical expressions developed for regimes of fast and slow interphase mass transport capture well the numerical model results at most model conditions. Some model trends we report here, such as improved current capability with increased polybromide phase volume fraction, have been observed experimentally. In the future a careful quantitative comparison between this theory and experimental data should be performed. Such careful comparisons can test model assumptions, and further allow for model-to-data fitting to extract key parameters such as the effective interphase mass transport coefficient. Overall, the models developed here will allow for deeper insight and design guidelines for a highly promising flow battery architecture for inexpensive energy storage.

Declaration of Competing Interest

The authors declare that they have no known competing financial interests or personal relationships that could have appeared to influence the work reported in this paper.

Declaration of Competing Interest

None.

Credit authorship contribution statement

R. Ronen: Formal analysis, Software, Writing – original draft. **A.D. Gat:** Formal analysis. **M.Z. Bazant:** Writing – review & editing. **M.E. Suss:** Supervision, Writing – review & editing.

Acknowledgments

The authors acknowledge financial support by the Binational Industrial Research and Development (BIRD) foundation, an MIT-Israel MISTI grant, and Israel Chemicals Ltd (ICL). This study is Supported by The Nancy and Stephen Grand Technion Energy Program (GTEP) and the Ministry of National Infrastructures, Energy and Water Resources via graduate student scholarships in the energy fields.

References

[1] World Energy Council, "Five steps to energy storage. innovation insights brief 2020," p. 62, 2020.
[2] A.A. Akhil, et al., DOE/EPRI 2015 electricity storage handbook in collaboration with NRECA, Sandia Nat. Lab. (January) (2015).
[3] B.R. Chalamala, T. Soundappan, G.R. Fisher, M.R. Anstey, V.V. Viswanathan, M.L. Perry, Redox flow batteries: an engineering perspective, Proc. IEEE 102 (6) (2014) 976–999.
[4] M. Skyllas-Kazacos, M.H. Chakrabarti, S.a. Hajimolana, F.S. Mjalli, M. Saleem, Progress in flow battery research and development, J. Electrochem. Soc. 158 (8) (2011) R55–R79.
[5] M.J. Mader, R.E. White, A mathematical model of a Zn/Br_2 cell on charge, J. Electrochem. Soc. 133 (7) (1986) 1297–1307.
[6] B. Li, et al., Ambipolar zinc-polyiodide electrolyte for a high-energy density aqueous redox flow battery, Nat. Commun. 6 (2015).
[7] A. Khor, et al., Review of zinc-based hybrid flow batteries: from fundamentals to applications, Mater. Today Energy 8 (8) (2018) 80–108.
[8] K. Lin, et al., Alkaline quinone flow battery, Science 349 (6255) (2015) 1529–1532.
[9] R. Ronen, I. Atlas, M.E. Suss, Theory of flow batteries with fast homogeneous chemical reactions, J. Electrochem. Soc. 165 (16) (2018) A3820–A3827.
[10] K.T. Cho, P. Albertus, V. Battaglia, A. Kojic, V. Srinivasan, A.Z. Weber, Optimization and analysis of high-power hydrogen/bromine-flow batteries for grid-scale energy storage, Energy Technol. 1 (10) (2013) 596–608.
[11] W.A. Braff, C.R. Buie, M.Z. Bazant, Boundary layer analysis of membraneless eectrochemical cells, J. Electrochem. Soc. 160 (11) (2013) A2056–A2063.
[12] K. Gong, F. Xu, M.G. Lehrich, X. Ma, S. Gu, Y. Yan, Exploiting immiscible aqueous-nonaqueous electrolyte interface toward a membraneless redox-flow battery concept, J. Electrochem. Soc. 164 (12) (2017) A2590–A2593.
[13] P. Leung, X. Li, C. Ponce De León, L. Berlouis, C.T.J. Low, F.C. Walsh, Progress in redox flow batteries, remaining challenges and their applications in energy storage, RSC Adv. 2 (27) (2012) 10125–10156.
[14] R. Ferrigno, A.D. Stroock, T.D. Clark, M. Mayer, G.M. Whitesides, Membraneless vanadium redox fuel cell using laminar flow, J. Am. Chem. Soc. 124 (44) (2002) 12930–12931.

[15] W.A. Braff, M.Z. Bazant, C.R. Buie, Membrane-less hydrogen bromine flow battery, Nat. Commun. 4 (2013) 1–6.
[16] H.S. Lim, A.M. Lackner, R.C. Knechtli, Zinc-bromine secondary battery, J. Electrochem. Soc. 124 (8) (1977) 1154–1157.
[17] M.E. Suss, K. Conforti, L. Gilson, C.R. Buie, M.Z. Bazant, Membraneless flow battery leveraging flow- through heterogeneous porous media for improved power density and reduced crossover, RSC Adv. 6 (102) (2016) 100209–100213.
[18] P. Leung, X. Li, C. Ponce de León, L. Berlouis, C.T.J. Low, F.C. Walsh, Progress in redox flow batteries, remaining challenges and their applications in energy storage, RSC Adv. 2 (27) (2012) 10125–10156.
[19] J.H. Yang, H.S. Yang, H.W. Ra, J. Shim, J.-D.D. Jeon, Effect of a surface active agent on performance of zinc/bromine redox flow batteries: improvement in current efficiency and system stability, J. Power Sources 275 (2015) 294–297.
[20] P.K. Leung, T. Martin, A.A. Shah, M.A. Anderson, J. Palma, Membrane-less organic-inorganic aqueous flow batteries with improved cell potential, Chem. Commun. 52 (99) (2016) 14270–14273.
[21] M. Schneider, G.P. Rajarathnam, M.E. Easton, A.F. Masters, T. Maschmeyer, A.M. Vassallo, The influence of novel bromine sequestration agents on zinc/bromine flow battery performance, RSC Adv. 6 (112) (2016) 110548–110556.
[22] M.E. Easton, A.J. Ward, B. Chan, L. Radom, A.F. Masters, T. Maschmeyer, Factors influencing the formation of polybromide monoanions in solutions of ionic liquid bromide salts, Phys. Chem. Chem. Phys. 18 (10) (2016) 7251–7260.
[23] G.D. Simpson, R.E. White, An algebraic model for a zinc/bromine flow cell, J. Electrochem. Soc. 136 (8) (1989) 2137–2144.
[24] L. Amit, D. Naar, R. Glouckhovski, G.J. O, M.E. Suss, A single-flow battery with multiphase flow, Chem. Sus. Chem, 14 (4) (2020) 1068–1073.
[25] Z. Xu, J. Wang, S.C. Yan, Q. Fan, P.D. Lund, Modeling of zinc bromine redox flow battery with application to channel design, J. Power Sources 450 (2) (2020) 227436.
[26] B. Koo, et al., Modeling the performance of a zinc/bromine flow battery, Energies 12 (6) (2019) 1159.
[27] T.I. Evans, R.E. White, A review of mathematical modeling of the zinc/bromine flow cell and battery, J. Electrochem. Soc. 134 (11) (1987) 2725–2733.
[28] E.E. Kalu, R.E. White, Zn/Br_2 cell: effects of plated zinc and complexing organic phase, AIChE J. 37 (8) (1991) 1164–1174.
[29] R.F. Probstein, Physicochemical Hydrodynamics: An Introduction, John Wiley & Sons, 2005.
[30] R.B. Bird, W.E. Steward, E.N. Lightfoot, Transport Phenomena (2002) Second..
[31] A. Nakayama, Y. Sano, X. Bai, A boundary layer analysis for determination of the limiting current density in an electrodialysis desalination, Desalination 404 (2017) 41–49.
[32] J.E. Dykstra, K.J. Keesman, P.M. Biesheuvel, A. van der Wal, Theory of pH changes in water desalination by capacitive deionization, Water Res. 119 (2017) 178–186.
[33] M. Mastragostino, S. Valcher, Polymeric salt as bromine complexing agent in a Zn-Br_2 model battery, Electrochim. Acta 28 (4) (1983) 501–505.
[34] M. Wegener, N. Paul, M. Kraume, Fluid dynamics and mass transfer at single droplets in liquid/liquid systems, Int. J. Heat and Mass Transf. 71 (2014) 475–495.
[35] D.J. Eustace, Bromine complexation in zinc-bromine circulating batteries, J. Electrochem. Soc. 127 (3) (1980) 528–532.
[36] J.M. Wimby, T.S. Berntsson, Viscosity and density of aqueous solutions of LiBr, LiCl, $ZnBr_2$, $CaCl_2$, and $LiNO_3$. 1. single salt solutions, J. Chem. Eng Data 39 (1) (1994) 68–72.
[37] G.P. Rajarathnam, M.E. Easton, M. Schneider, A.F. Masters, T. Maschmeyer, A.M. Vassallo, The influence of ionic liquid additives on zinc half-cell electrochemical performance in zinc/bromine flow batteries, RSC Adv. 6 (33) (2016) 27788–27797.
[38] S. Whitkar, The transport equations for multi-phase systems, Chem. Eng. Sci. 28 (1) (1973) 139–147.
[39] W.G. Gray, A derivation of the equations for multi-phase transport, Chem. Eng. Sci. 30 (2) (1975) 229–233.
[40] J. Newman, W. Tiedemann, Porous-electrode theory with battery applications, AIChE J. 21 (1) (1975) 25–41.
[41] S. Whitaker, Introduction to Fuid Mechanics, 56, Krieger Pub Co, 2012.
[42] B.R. Locke, Electrophoretic transport in porous media: a volume-averaging approach, Ind. Eng. Chem. Res. 37 (2) (1998) 615–625.
[43] V.P. Nemani, K.C. Smith, Robust simulation of coupled reactions and transport in redox flow batteries using tailored numerical schemes, J. Electrochem. Soc. 167 (10) (2020) 103504.
[44] A. Apelblat, Mass transfer with a chemical reaction of the first order. Effect of axial diffusion, Chem. Eng. J. 23 (2) (1982) 193–203.
[45] W.M. Deen, Analysis of Transport Phenomena, Oxford University Press, 1998.
[46] P.L. Chambré, J.D. Young, On the diffusion of a chemically reactive species in a laminar boundary layer flow, Phys. Fluids 1 (1) (1958) 48–54.
[47] A.Z. Weber, J. Newman, Modeling transport in polymer-electrolyte fuel cells, Chem. Rev. 104 (10) (2004).
[48] P. C. Butler, P. A. Eidler, P. G. Grimes, S. E. Klassen, and R. C. Miles, "Zinc/bromine batteries," *Handbook of Batteries* (Ed.: David Linden, Thomas B. Reddy), McGraw-Hill, Ohio, vol. Chapter 37, 2001.
[49] J. Lee, J. Hwang, J. Chang, Quantitative determination of chemical species in high concentration ZnX_2 (X = Br and I) media by steady state voltammetry on Pt ultramicroelectrode, J. Electroanal. Chem. 808 (2018) 141–149.
[50] S. Azzopardi, F. Hills, B. Brauner, M. Celata, P. Marchioli, Modelling and experimentation in two-phase flow, Springer (450) (2003).
[51] D.J. Eustace, Bromine complexation in zinc-bromine circulating batteries, J. Electrochem. Soc. 127 (3) (1980) 528–532.
[52] D.C. Constable, K.J. Cathro, K. Cedzynska, P. Melbourne, Some properties of zinc/bromine battery electrolytes, J. Power Sources 16 (1985) 53–63.
[53] S.R. Derkach, Rheology of emulsions, Adv. Colloid Interface Sci. 151 (1–2) (2009) 1–23.